

# Shear Band Formation and Mode II Fracture of Polymeric Glasses

Jared S. Archer, Alan J. Lesser

Polymer Science and Engineering Department, University of Massachusetts, Amherst, Massachusetts 01003

Correspondence to: A. J. Lesser (E-mail: [ajl@polysci.umass.edu](mailto:ajl@polysci.umass.edu))

Received 11 January 2010; revised 27 August 2010; accepted 9 September 2010; published online 11 November 2010

DOI: 10.1002/polb.22159

**ABSTRACT:** Mode I and II fracture studies were performed from quasistatic to low velocity impact rates on polymethyl methacrylate (PMMA) and polycarbonate (PC). Mode II tests used an angled double-edge notched specimen loaded in compression. The shear banding response of PMMA is shown to be highly sensitive to rate, with diffuse shear bands forming at low rates and sharp distinct shear bands forming at high rates. As the rate increases, shear deformation becomes more localized to the point where Mode II fracture occurs. PC is much less rate dependent and stable shear band propagation is observed over the range of rates studied with lesser amounts of localization. A new theory is formulated relating orientation in a shear

band to intrinsic material properties obtained from true-stress true-strain tests. In a qualitative sense the theory predicts the high rate sensitivity of PMMA. A kinematic limit for orientation within a shear band is also derived based on entanglement network parameters. Mode II fracture in PMMA is shown to occur at this kinematic limit. For the case of PC, the maximum impact rates were not high enough to reach the kinematic limit. © 2010 Wiley Periodicals, Inc. *J Polym Sci Part B: Polym Phys* 49: 103–114, 2011

**KEYWORDS:** fracture; glassy polymers; Mode II; PMMA; polycarbonates; shear band; structure-property relations

**INTRODUCTION** Polymethyl methacrylate (PMMA) and polycarbonate (PC) have been used throughout the literature as model glassy polymers. From a fracture mechanics perspective, these two materials offer a nice contrast in fracture mechanisms. Typically, PMMA fails in a brittle fashion while PC deforms in a ductile manner. The plastic deformation that accompanies the ductile failure process in PC absorbs large amounts of energy leading to higher impact energy absorption than brittle PMMA. However, this is not always the case. Song and coworkers have shown that at ballistic rates and high plate thicknesses, PMMA outperforms PC.<sup>1</sup> At the high rates where this crossover occurs, surface area created during radial cracking in PMMA is reduced and the failure pattern is more localized. This is a curious result in that the dominant energy absorption mechanism in brittle fracture is the creation of surface area. If the damage area decreases, one would expect a decrease in energy absorption rather than the observed increase. To further understand this behavior, we will explore the change in fracture properties as a function of rate.

A similar result has been reported in the authors' work on the impact resistance of prestressed PMMA.<sup>2</sup> Under a compressive prestress, the failure stress increases and impacted plates display minimal radial cracking. The most striking result is that the failure stress increase is significantly higher when samples are subjected to a shear prestress in addition to a compressive prestress. It is clear from these results that stress state can affect the fracture properties. What remains

unclear is whether or not shear prestress can induce mixed mode fracture. Moreover, if a Mode II mechanism is excited, what effect will it have on fracture properties? The examples given in refs. 1 and 2 both involve a circularly supported plate impacted normal to the surface. During impact, fracture can initiate on the contact surface or on the distal surface. Separating the effects of different fracture Modes becomes difficult in these types of tests. To simplify interpretation, we will investigate the rate effects on Mode I and Mode II fracture separately.

The characterization of Mode I fracture is relatively straightforward and standard techniques are used in this work. However, there are issues surrounding Mode II fracture in polymers that warrant further background and explanation.

## Mode II Fracture

The general approach to achieve Mode II fracture is to apply a critical shear stress to a precracked specimen. If Mode II fracture occurs, a crack should propagate along the direction of the precrack. However, the typical response is propagation via a Mode I kink.<sup>3,4</sup> This behavior is nicely illustrated by Figure 1, which shows a PMMA Cracked Brazilian Disc loaded in compression under pure Mode II conditions (the experiment was performed by the authors). Rather than growing collinear with the diametral precrack, the cracks initiate at an approximate angle of 72° relative to the precrack. During propagation the path of the crack curves in the direction of the loading axis and by doing so, minimizes

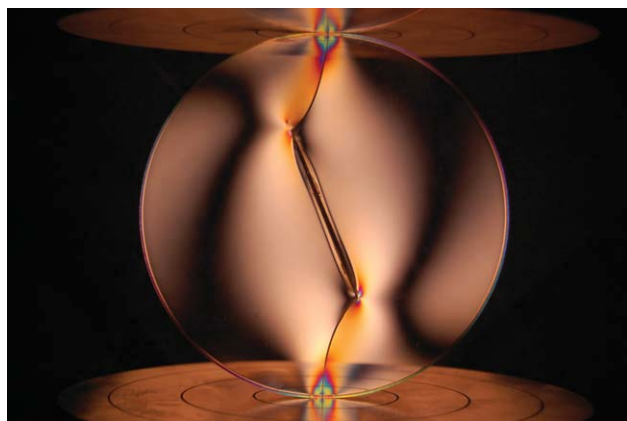


**FIGURE 1** Cracked Brazilian Disc of PMMA loaded in pure Mode II. Mode I cracks initiate at an angle of  $72^\circ$  relative to the pre-crack as predicted by the MTS criterion illustrating that  $K_{IIC} > K_{IIC}$ . Disc diameter = 101 mm.

the amount of shear stress at the crack tip. This observation that precracks loaded under shear propagate at some angle to the precrack led to the development of the Maximum Tangential Stress (MTS) criterion of Erdogan and Sih.<sup>5</sup> This theory essentially states that a loaded precrack will grow in the direction in which the tangential stress is the highest and therefore, will proceed through a Mode I dominate mechanism. This suggests that for most materials, the Mode I fracture toughness,  $K_{IIC}$ , is less than the Mode II fracture toughness,  $K_{IIC}$ . If this is the case, a necessary condition for achieving Mode II fracture is suppression of Mode I fracture. Accordingly, Melin posited that a precrack loaded under Mode II conditions will extend without Mode I kinking if the in plane compressive stresses are high enough to suppress Mode I fracture.<sup>6</sup> Broberg experimentally verified this prediction by loading a precracked plate of PMMA under biaxial compression.<sup>7</sup> The rate of loading was not specified but was likely in the quasistatic range. This is generally agreed to be the first evidence of the realization of Mode II fracture in a polymer. Values of  $K_{IIC}$  were shown to be  $\sim 2.5$  times higher than  $K_{IIC}$ .

Other examples from the literature have shown that a transition to Mode II fracture can also occur at high loading rates. Kalthoff used the shadow optical method of caustics to investigate dynamic Mode II loading in high strength maraging steel.<sup>8</sup> At low loading rates ( $\sim 10$  m/s) cracks would grow under Mode I conditions at an approximate angle of  $70^\circ$  as predicted by the MTS criterion. However, above some critical loading rate the failure mechanism changed from a Normal Stress dominated failure to that initiated by shear bands extending in the direction of the precracks. Ravi-Chandar et al. took a similar approach to Kalthoff and studied PMMA and PC.<sup>9</sup> Their work used photoelasticity and high speed imaging to measure the dynamic fracture toughness of both materials. A rate dependent transition to Mode II fracture was also observed.

The motivation for this work is to investigate in depth the rate-dependent material properties that can lead to Mode II

fracture in glassy polymers. Since shear bands are the precursor to Mode II fracture, we will characterize the effect of rate on shear band formation. We will also develop conditions for shear band stability based on both a force balance and a kinematic approach.

## MATERIALS

The PMMA used was Acrylite GP purchased from K-Mac Plastics. The PC was Tuffak general-purpose grade supplied by Arkema.

## EXPERIMENTAL

### Mode I Fracture

To test Mode I properties a three point bend specimen was used. Samples were machined to nominal dimensions of  $28 \times 85 \times 6$  mm. Precracks were made at the center of the 85 mm edge with nominal length of 14 mm. The precrack was formed by first making a cut with a diamond saw and then a sharp crack tip was achieved by taping a razor blade in the slot with a hammer. Three point bend tests were conducted on an Instron 5800 at quasistatic crosshead displacement rates and on a Dynatup 8250 at low-velocity impact rates. The crosshead displacement rates tested were 0.1, 1, 10, 100, 100k, 148k, 196k, and 245k mm/min, where  $k = 1000$ . The first four rates were within the capabilities of the Instron while the final four made use of the Dynatup with a 3.27 kg mass. The loading pins were 6 mm in diameter with exception of tests performed on the Dynatup, where a 9.5 mm diameter hemispherical tup impacted the sample. The span of the bottom loading pins was 60 mm. Testing was done at standard ambient conditions of  $23^\circ\text{C}$  and 50% relative humidity.

### Mode II Deformation and Fracture

Mode II specimens were machined to rectangular shapes with nominal dimensions of  $13 \times 85 \times 6$  mm (Fig. 2). Each specimen was precracked from both edges at an angle of  $45^\circ$  so that the center of the area between the precracks was  $\sim 38$  mm from one edge. The precrack was formed by the same method as the three point bend specimens. The total precrack length was on the order of 13 mm. The specimen was loaded in compression along the axis corresponding to the 85 mm dimension. To prevent buckling of the sample during compressive loading, a simple steel support jig was used during testing at all rates (Fig. 3). The sample was aligned so that the area between the precracks was visible in the viewing hole. The four screws were finger tightened to lightly secure the sample without significantly restricting deformation during testing. When the sample was loaded in

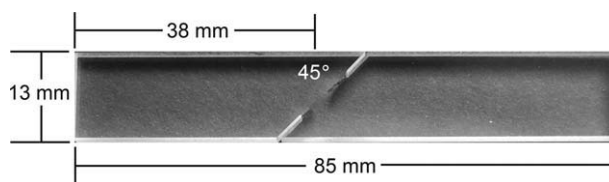


**FIGURE 2** Mode II sample dimensions. Thickness = 6 mm.

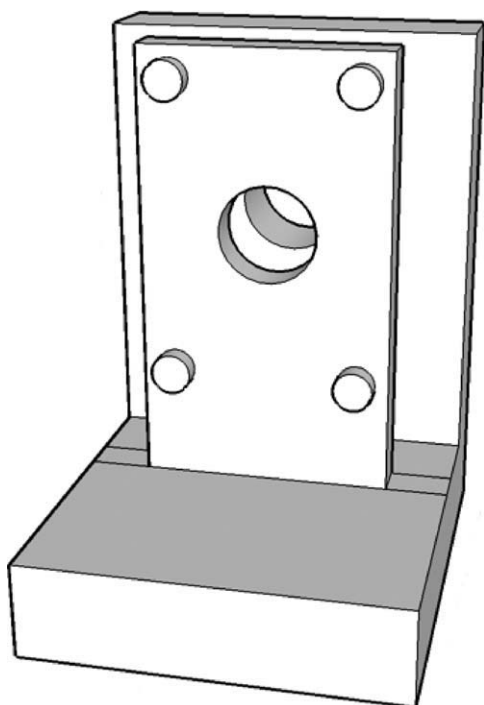


FIGURE 3 Support jig for Mode II tests.

the jig,  $\sim 10$  mm of length was left unsupported to allow for adequate axial compression of the sample. Compressive crosshead displacement rates ranging from 0.1–500 mm/min were achieved in an Instron 5800. For testing at rates up to 253 k mm/min, a Dynatup 8250 was used. To measure the shear strain within the shear bands, a series of lines normal to the plane of the shear band were drawn on the surface. During the shear banding tests, images were taken at known time intervals. For crosshead displacement rates less than 100 mm/min, a digital still camera was used to capture the images. The time interval between images from the still camera was determined by two methods. At a crosshead displacement rate of 0.1 mm/min, a timer with an LCD showing elapsed seconds was placed next to the sample so that each image contained the time difference to the nearest second. This gave adequate precision considering the deformation takes place over 30 minutes. For crosshead displacement rates from 1–32 mm/min, a dial indicator displaying crosshead displacement was placed so that its reading was contained in each image. The time interval between images was calculated using the crosshead displacement rate and the change in the displacement between images. For crosshead displacement rates 100 mm/min and higher, a high speed camera was used to capture the images. The time interval between images was determined by the camera frame rate. The local maximum shear strain rate in the shear band was calculated by measuring the shear strain in the images and plotting this against time (Fig. 4). A sigmoidal curve was fit to the data, and then this function was differentiated to arrive at the shear strain rate. This curve was also used to define the maximum shear strain,  $\gamma_{\max}$ .

Low frame rate imaging of the samples during testing was captured with a Nikon D40 digital SLR camera. High speed

imaging was performed on a Kodak Ektapro HS4540. Frame rates from 30–40,500 fps were used.

### Compression

True stress–true strain compression tests were performed on both PMMA and PC over a range of temperatures and strain rates. Cylindrical samples were machined from sheet stock using a hole-cutting end mill with an inner diameter of 4.4 mm. The machining was done in a water bath to prevent excessive heating and consequent orientation at the machined surface. One end of the cylinder was then machined and wet polished with a polishing wheel using successively smaller grit down to 9 micron. Nominally, the final dimensions were height = diameter = 4.35 mm. To ensure affine deformation, each end of the cylinder was covered with PTFE tape and a drop of lubricant was placed on each compression platen. For PMMA, silicone oil was used as a lubricant. For PC, uncrosslinked polydimethyl siloxane (PDMS) with molecular weight of 6000 g/mol was used. These silicone based lubricants were used rather than a water-surfactant mixture because of low temperature testing. PDMS was used for PC to avoid environmental stress cracking. The test temperatures were 23,  $-20$ , and  $-60$  °C. Temperature was controlled with an oven using a Thermcraft controller and liquid nitrogen as the coolant. Samples were allowed to equilibrate at the test temperature for 1 h prior to testing. The load cell was maintained at room temperature during low temperature testing by wrapping the adjacent section of the load train with heating tape. The constant strain rates used were 0.01, 0.1, and  $1 \text{ min}^{-1}$ . The analysis of the data took into consideration the load train compliance, which was measured to be  $2.40 \times 10^{-8} \text{ m/N}$ . The material properties measured from these tests were the yield stress,  $\sigma_y$ , rejuvenated stress,  $\sigma_r$ , the strain hardening modulus,  $G_R$ , and the strain localization parameter  $k_y = \sigma_y / \sigma_r$  (Fig. 5).

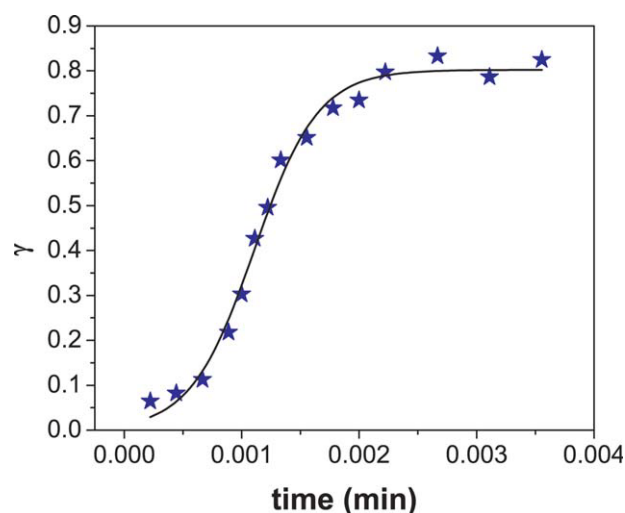
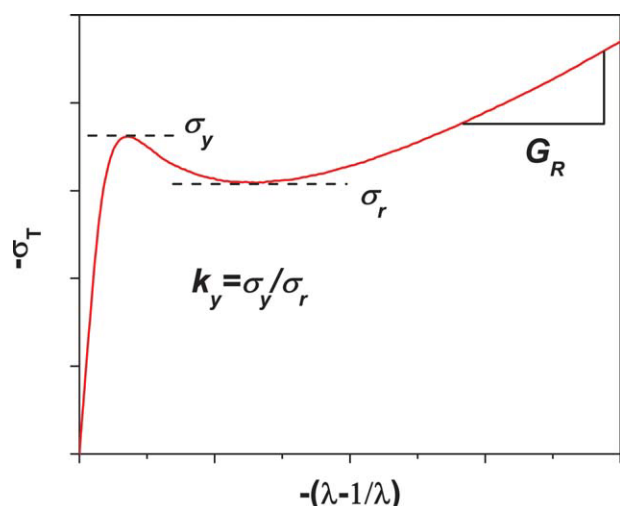


FIGURE 4 Shear strain vs. time used to calculate maximum shear strain rate and maximum shear strain.



**FIGURE 5** Intrinsic material properties obtained from true-stress true-strain compression tests.  $\sigma_y$ ,  $\sigma_r$ ,  $G_R$ , and  $k_y$  represent the yield stress, rejuvenated stress, strain hardening modulus and strain localization parameter respectively.

$\sigma_y$  and  $\sigma_r$  were determined from the local maxima and minima shown in Figure 5.  $G_R$  was determined from a linear regression of the data in the extension range;  $-(\lambda-1/\lambda) = 1.5:2$ .

## RESULTS AND DISCUSSION

### Mode I

#### PMMA

The effect of rate on Mode I fracture toughness has been studied before and the results shown here are typical of those reported in the literature.<sup>10,11</sup> In the quasistatic range, the Mode I fracture toughness of PMMA shows modest

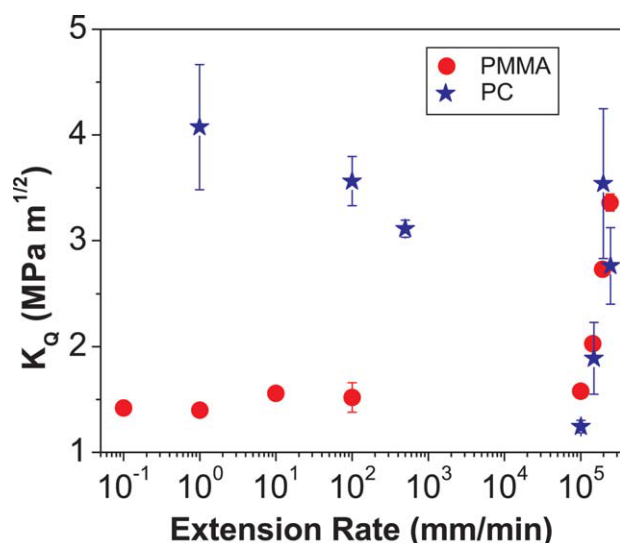


**FIGURE 6** Mode I fracture toughness of PMMA and PC.

increases with rate (Fig. 6). Above a rate of  $10^5$  mm/min, the fracture toughness increases rapidly with rate. There is a corresponding shift in crack propagation stability and fracture morphology (Fig. 7). At lower rates, crack growth is stable and morphologically the surface contains striations in the direction of crack growth along with fan markings toward the end of the crack. As impact speed increases, crack growth becomes more unstable as evidenced by lines of crack arrest on the surface. At the highest impact speeds, crack growth is unstable and the fractured surface shows parabolic markings associated with the initiation of secondary cracks ahead of the primary crack front.<sup>2,12,13</sup> With the onset of these parabolic markings comes the drastic increase in fracture toughness. This high rate response is significant to this work in that it suggests an additional route to achieving Mode II fracture. In the shear banding experiments outlined in the following sections, Mode I failure is suppressed by the compressive stress normal to the plane of interest. If by increasing the impact rate, the Mode I fracture toughness can be increased such that  $K_{IC} > K_{IIC}$ , Mode II will be the preferred fracture mechanism.

### PC

At low rates, the Mode I fracture toughness of PC exceeds that of PMMA by a factor of  $\sim 2.6$  (Fig. 6). At these rates, the deformation behavior is highly ductile. As rate is increased there is a decrease in fracture toughness until the rate of  $10^5$  mm/min. At the crosshead displacement rate of 1 mm/min, PC undergoes ductile failure while at 500 mm/min, every sample fails in a brittle fashion. This ductile to brittle transition can be explained in terms of the Ludwig-Davidenkov-Orowan hypothesis.<sup>14</sup> This is simply a comparison of the effect of rate (or temperature) on the yield stress and the brittle fracture stress. At low rates, the yield stress is lower than the brittle fracture stress and the specimen will fracture

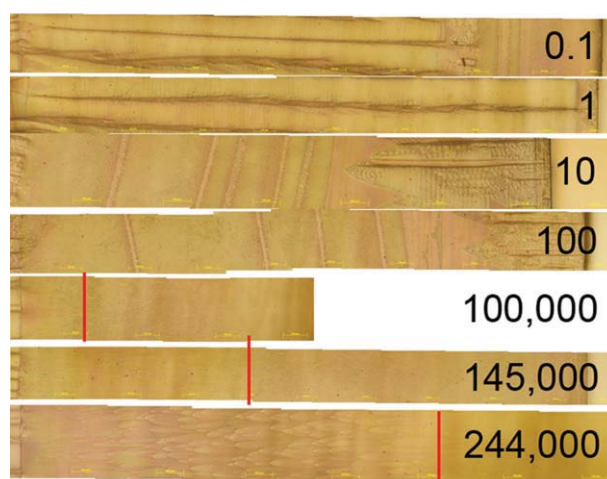


**FIGURE 7** Mode I fracture surface morphology in PMMA. Numbers indicate impact rate in mm/min. Crack growth is from left to right. Vertical lines in bottom three images indicate boundary of parabolic markings. The height of each image = 1.3 mm.



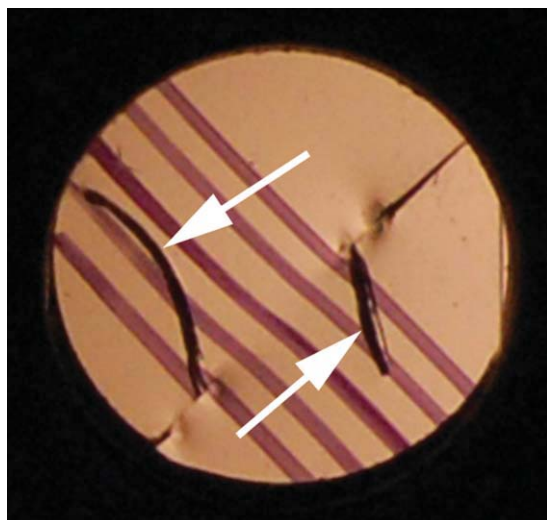


**FIGURE 8** Arrows indicate Mode I kinks. Diameter = 12.7 mm.

in a ductile manner. As the rate increases, so does the yield stress until a point where it exceeds the brittle fracture stress and a transition to brittle fracture is observed. At this point, a sharp increase in fracture toughness is observed similar to the response of PMMA (Fig. 6).

#### Mode II

At low crosshead displacement rates, a stable shear band forms connecting the two precracks. As a consequence of this deformation, the material is locally oriented in the first principal direction. The width of the shear band increases and more material is drawn into the band as a consequence

of the strain hardening response. This general process holds many similarities to necking seen in tensile tests of polymers. We will take advantage of these similarities later when we develop the condition of shear band stability.

One advantage of the specimen geometry is that, when under a compressive load, the plane containing the two precracks experiences the maximum shear stress in addition to a compressive stress normal to the plane. This compression suppresses Mode I cracks in the plane of interest. However, tensile stresses do develop at the crack tip and reach a maximum at  $\sim 65^\circ$  with respect to the precrack plane, as evidenced by the Mode I kinks that form in PMMA (Fig. 8). Another advantage of the geometry is that even in the presence of Mode I kinks, the sample still carries a load and the shear stress can continue to increase.

#### PMMA

At shear strain rates from  $0.2\text{--}394\text{ min}^{-1}$ , stable shear bands are formed in PMMA with no Mode II fracture (Figs. 9 and 10). As the rate is increased, the maximum shear strain in the band increases as the width of the band narrows. At crosshead displacement rates of  $500\text{ mm/min}$  and higher, Mode II fracture is observed.

For the tests performed in the Dynatup on PMMA, following the Mode II fracture event, the two newly formed surfaces reseal and the load again rises until either all the kinetic energy of the falling mass is spent and the tup rebounds or fracture initiates at the tup-sample contact point.

Occasionally, due to contact stresses, the top portion of the sample will fracture prior to complete Mode II fracture. When this occurs, the release of the load is so quick that it provides a snapshot of the Mode II fracture process.

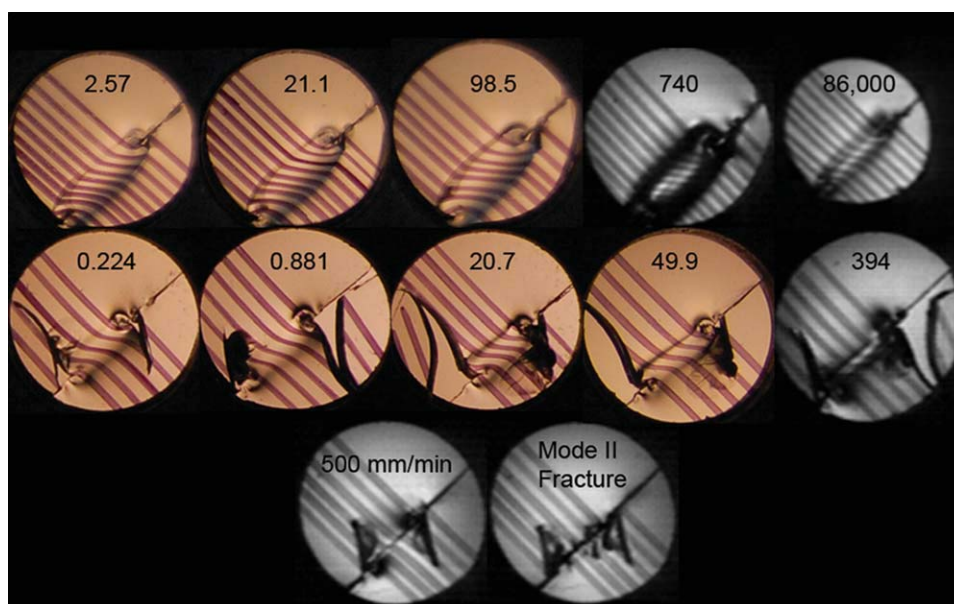


**FIGURE 9** Effect of rate on shear band formation. First row PC, second and third rows PMMA. Numbers in first two rows indicate shear strain rate in  $\text{min}^{-1}$ . Diameter in each image = 12.7 mm.

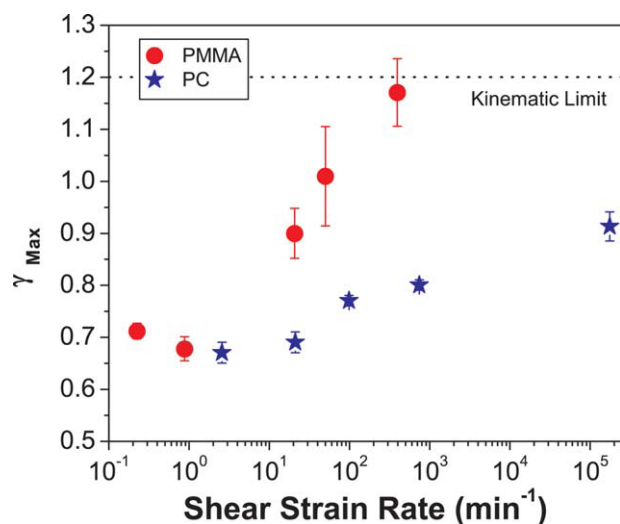


FIGURE 10 Maximum shear strain vs. shear strain rate.

Figure 11 is a striking example of this. The end of one precrack is shown in the top left hand corner of the image while the end of the other precrack is just out of view in the opposite corner. The series of black lines oriented at  $45^\circ$  are for reference and were made by tapping a stack of razor blades onto the surface prior to testing. Shear bands can be seen propagating from the tip of each precrack. The one on the left side of the image is easily identified as a shear band rather than a Mode I crack by noting the resultant offset in the surface reference lines. The shear band on the right side

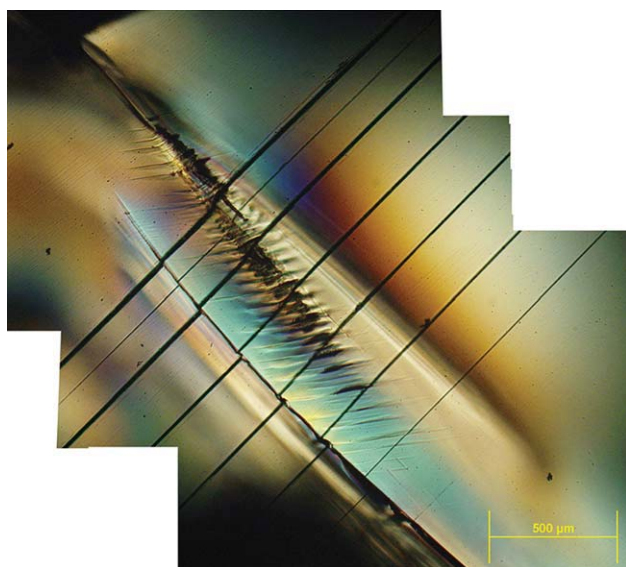


FIGURE 11 PMMA prior to complete Mode II fracture viewed under crossed polars. Black lines at  $45^\circ$  are surface marks for surface displacement reference. Shear band is identified by offset in reference lines. Shallow micro-tensile cracks form at  $\sim 45^\circ$  to shear bands. Scale bar =  $500\ \mu\text{m}$ .

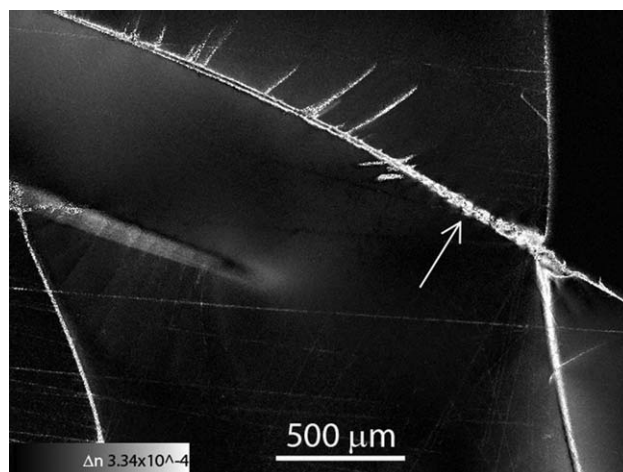


FIGURE 12 Map of birefringence of shear bands in PMMA prior to complete Mode II fracture. The level of birefringence is represented by the continuous grayscale in the image (black = 0, white =  $3.34 \times 10^{-4}$ ). Spatial scale bar =  $500\ \mu\text{m}$ . The arrow indicates the location for the line scan of birefringence shown in Figure 13.

had not yet reached the surface and shows no noticeable perturbation of the reference lines. The relative orientation and width of the shear band was measured by analyzing the birefringence of a cross section of the sample with a LC-Pol-scope Pro imaging system (Fig. 12). The width of the shear band is on the order of  $100\ \mu\text{m}$ . The maximum birefringence is above  $2.5 \times 10^{-4}$  while outside the shear band the orientation is negligible (Fig. 13). This data shows that in the early stages of shear band formation, the deformation is highly localized. Between the two shear bands there is a series of horizontal features that because of their orientation to the applied stress field are believed to be microtensile cracks. These cracks were only found on the surface shown in Figure 11 and were analyzed using fluorescent penetrant

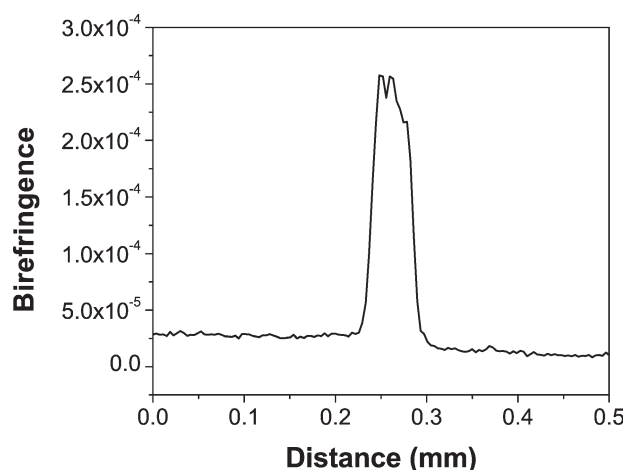


FIGURE 13 Line scan of birefringence of shear band in PMMA.

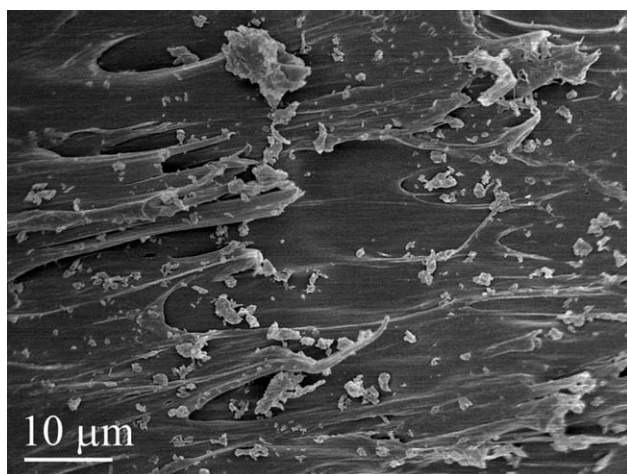


FIGURE 14 SEM image of Mode II fracture surface of PMMA.

dye and confocal microscopy. The deepest of such cracks propagated to a depth of  $\sim 100 \mu\text{m}$ . The presence of these microcracks begs the question, is fracture proceeding through a Mode I process? The fracture mechanism of samples loaded in Mode II is frequently described as the coalescence of microtensile cracks rather than a shearing process, which should accompany true Mode II fracture.<sup>15,16</sup> Because of the shallow depth of the microcracks and their presence on only one surface, they are likely to have developed at the end of the process. In contrast, the shear bands occupy nearly the entire 6 mm of thickness and have grown past each other. Further evidence of Mode II fracture lies in the fracture surface morphology. The process of microtensile crack coalescence leaves a characteristic hackled surface morphology. The SEM image in Figure 14 shows the Mode II fracture surface, which does not have a hackled appearance. The surface shows evidence of flowing material indicative of a shearing process.

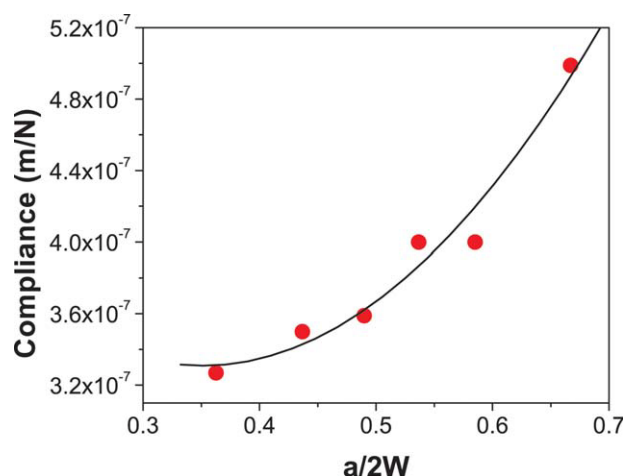


FIGURE 15 Relationship of sample compliance to crack length for Mode II specimens.

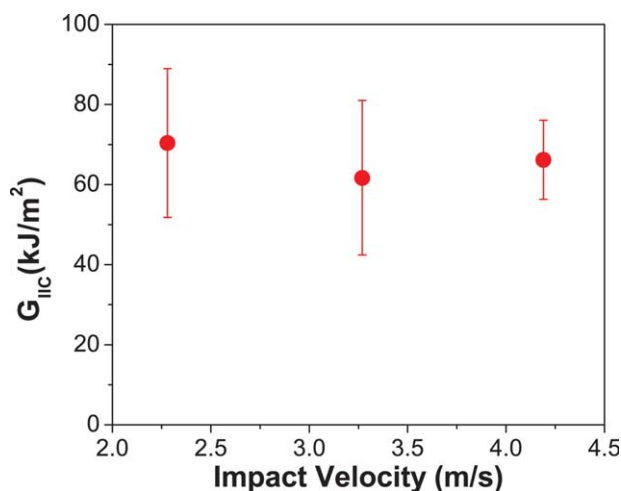


FIGURE 16 Mode II critical strain energy release rate for PMMA.

To determine the critical strain energy release rate,  $G_{IIc}$ , samples were prepared with a range of precrack lengths and the sample compliance was measured in an Instron. The data points from the compliance measurements were plotted against  $a/2W$ , where  $a$  is the crack length and  $W$  is the width (Fig. 15). The polynomial fit to this data is used to determine  $\partial C/\partial a$  and allows one to arrive at an expression for  $G_{IIc}$ .

$$G_{IIc} = \frac{P^2}{2b} \frac{\partial C}{\partial a} = \frac{P^2}{2b} \left( C_1 \frac{a}{W^2} + C_2 \frac{1}{W} \right) \quad (1)$$

The fit gave the values for the constants  $C_1$  and  $C_2$  of  $8.10 \times 10^{-7}$  and  $-5.70 \times 10^{-7}$ , respectively. Using eq 1 and the

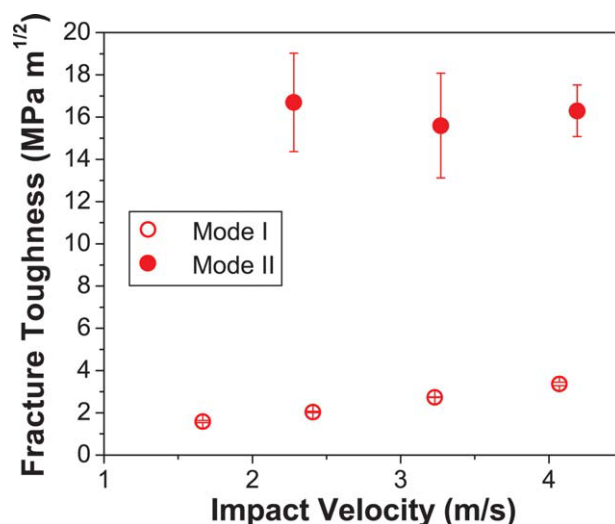


FIGURE 17 Comparison of Mode I and II fracture toughness in PMMA.



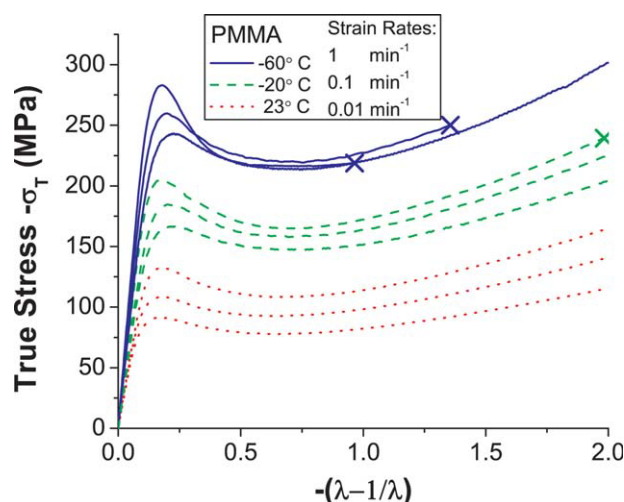


FIGURE 18 True-stress true-strain response of PMMA.

critical failure loads,  $G_{IIC}$  for PMMA was calculated for three different rates (Fig. 16). Over the range of velocities tested there is no clear correlation between  $G_{IIC}$  and impact velocity. Strain energy release rate can be related to fracture toughness in the case of plane strain using the relation,

$$G = \frac{K^2(1 - \nu^2)}{E} \quad (2)$$

From the data presented in Figure 17,  $K_{IIC}/K_{IC} \sim 6.7$ . This value is a lower estimate since the values for modulus and Poisson's ratio used were measured at quasistatic rates. This result is of great practical significance since it suggests that if one were to suppress Mode I fracture completely, the increases in fracture toughness would be substantial. Previous work by the authors has looked at suppressing Mode I fracture through the superposition of a compressive prestress.<sup>2</sup> In those results, even though Mode I fracture was not suppressed completely, significant improvements in impact strength occurred when a shear prestress was superposed with the compressive prestress.

### PC

Qualitatively, the shear band response of PC is similar to that of PMMA in that both show increased shear strain with increased loading rate (Fig. 9). However, the rate dependence of PC is significantly lower than PMMA (Fig. 10). Over the entire range of rates, PC was able to form a stable shear band and Mode II fracture was not observed.

### Intrinsic Material Properties

The true-stress true-strain experiments allow for the determination of intrinsic material properties such as the yield stress,  $\sigma_y$ , rejuvenated stress,  $\sigma_p$ , and the strain hardening modulus,  $G_R$  (Figs. 5, 18, and 19). These parameters have been used by several authors including Haward, Meijer,

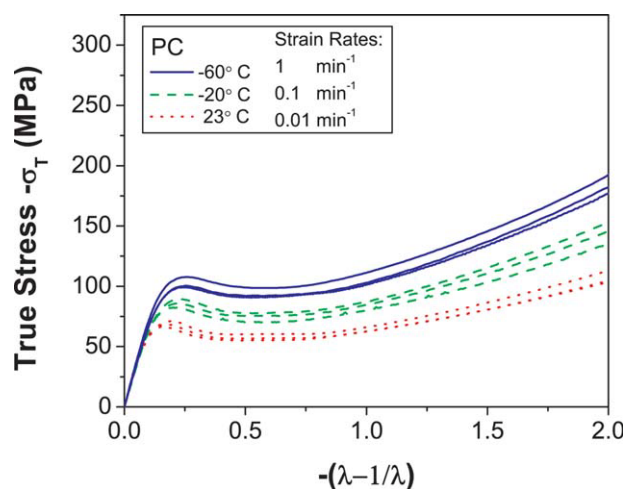


FIGURE 19 True-stress true-strain response of PC.

Govaert, and Boyce to describe necking behavior in polymers.<sup>17–19</sup> We will now develop the condition for shear band stability based on these intrinsic material properties.

### Condition for Shear Band Stability

As noted earlier, there are some qualitative similarities between shear band and neck growth. In the general sense, once either process has been initiated, propagation proceeds in a self-similar manner as more material is drawn into the oriented state. Taking advantage of these similarities, we will now develop the condition for shear band stability. The key assumptions in this development are: no change in cross-sectional area during deformation and material incompressibility. In essence this is a force balance between the applied

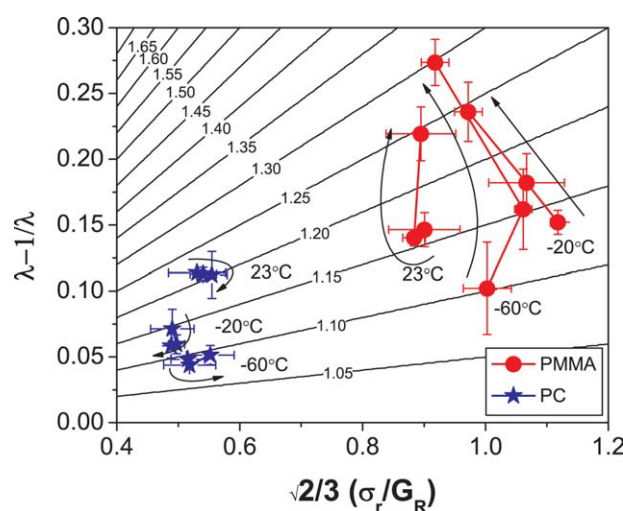


FIGURE 20 Predicted relationship between intrinsic material properties and orientation within a shear band. Contour lines represent steps in  $k_\gamma$ . Arrows indicate direction of increasing strain rate.



**TABLE 1** Required Temperature Increase to Achieve Observed Orientation for PC

$\dot{\gamma}$ (min <sup>-1</sup> )	$\gamma$	$G_R^{\text{calc}}$ (MPa)	Required $\Delta T$ (K)	Mechanical Energy (J)	Mass in Shear Band (mg)	Estimated $\Delta T$ (K)
2.57	0.67	7.6	77	6.09	133	6
21.1	0.69	7.3	78	3.95	150	3
98.5	0.77	6.5	79	8.47	171	6
740	0.80	6.3	80	7.99	155	7

farfield shear stress and the true shear stress in the shear band,  $\tau_0 A_0 = \tau A$ . From incompressibility,  $\lambda_1 \lambda_2 \lambda_3 = 1$  and from constant cross sectional area,  $\lambda_1 \lambda_3 = 1$  and  $\lambda_2 = 1$ . Let  $\lambda_1 = \lambda$ ,  $\lambda_3 = 1/\lambda$ . From rubber elasticity,

$$f = \frac{1}{2} G_R (\lambda_1^2 + \lambda_2^2 + \lambda_3^2 - 3) \quad (3)$$

where  $f$  is the strain energy density,  $G_R$  is the strain hardening modulus and  $\lambda_i$  is the extension ratio in the  $i$  direction. After substitution,

$$f = \frac{1}{2} G_R \left( \lambda - \frac{1}{\lambda} \right)^2 \quad (4)$$

Let,

$$\gamma = \lambda - \frac{1}{\lambda} \quad (5)$$

where  $\gamma$  is the shear strain. Differentiating to obtain the true shear stress,

$$\tau = \frac{\partial f}{\partial \gamma} = G_R \left( \lambda - \frac{1}{\lambda} \right) \quad (6)$$

Stable shear band propagation will occur after strain softening and at a farfield stress of  $\tau_0 = \tau_y$ . The force balance is then,  $\tau_0 A_0 = \tau_y A_0 = \tau A$ . If there is no change in cross-sectional area, then  $A_0 = A$  and  $\tau_y = \tau$ . After strain softening,

$$\tau_y = \tau_r + G_R \left( \lambda - \frac{1}{\lambda} \right) \quad (7)$$

Introducing the strain softening parameter,  $k_y = \tau_y/\tau_r$

$$\tau_y = \frac{\tau_y}{k_y} + G_R \left( \lambda - \frac{1}{\lambda} \right) \quad (8)$$

Rearranging and substituting for the octahedral shear stress,  $\tau_{\text{oct}} = \sqrt{2}\sigma_y/3$

$$\frac{\sqrt{2}\sigma_y}{3G_R} = \frac{\lambda - \frac{1}{\lambda}}{1 - \frac{1}{k_y}} \quad (9)$$

This relationship allows one to relate the intrinsic material properties;  $\sigma_y$ ,  $\sigma_p$  and  $G_R$  to the amount of orientation in a shear band. This is shown graphically in Figure 20. The material properties derived from true-stress true-strain compression tests are used to predict the corresponding orientation within the shear band. During the testing of PMMA at lower temperatures, failure occurred prior to the onset of strain hardening disallowing the calculation of  $G_R$ . In these cases, a master curve of  $G_R$  versus strain rate was used to extrapolate the values of  $G_R$ .

In a qualitative sense, the trends seen in Figure 20 for PMMA match the experimentally observed results. An increase in strain rate produces a shear band with higher orientation. For PC, the opposite trend is observed. The model predicts a decrease in orientation with an increase in strain rate. This is clearly contrary to the observed behavior in Figure 10. One possible source for the discrepancy between the predicted and experimental behavior of PC is that to estimate the response at high rates, tests were run at lower temperatures. These temperatures begin to approach the  $\beta$  transition of PC ( $T_\beta = -100$  °C).<sup>20</sup> Quantitatively, the amount of orientation predicted by the model is significantly lower than the measured amounts of shear strain. Care should be taken in making comparisons between the predicted behavior and the experimentally produced shear bands. The material properties were obtained during isothermal affine deformation at constant strain rate. In contrast, the shear

**TABLE 2** Required Temperature Increase to Achieve Observed Orientation for PMMA

$\dot{\gamma}$ (min <sup>-1</sup> )	$\gamma$	$G_R^{\text{calc}}$ (MPa)	Required $\Delta T$ (K)	Mechanical Energy (J)	Mass in Shear Band (mg)	Estimated $\Delta T$ (K)
0.224	0.71	12	43	3.5	79	7
0.881	0.68	16	37	10.0	78	20
21.0	0.90	21	29	7.3	57	20
50.0	1.01	22	27	4.0	57	11
394	1.17	26	21	0.8	27	5

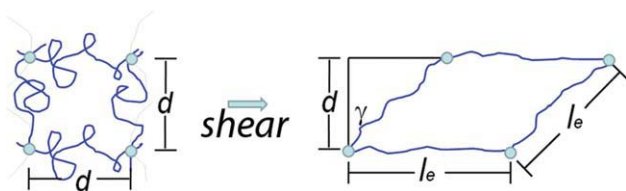


**FIGURE 21** Molecular network parameters used to define  $\gamma_{\max}$  in shear.

banding experiments likely violate each of these constraints. The conditions of affine deformation and constant strain rate are clearly not met during the shear banding experiments. Since shear banding involves plastic deformation it is reasonable to expect a corresponding increase in temperature especially at the higher rates.<sup>21</sup> If the temperature does increase during the test by a significant amount, the value of  $G_R$  used to predict the response would be artificially high and the model would predict a lower level of orientation.

To see if temperature effects could explain some of the discrepancy between the model and the experimental results, a simplified analysis was performed. The approach taken was to consider if all the mechanical energy put into the sample during shear deformation was converted to heat, would this be enough energy to raise the temperature to get a value of  $G_R$  that would correspond to the observed amount of orientation. The first step in the analysis is to calculate this value of  $G_R$ ,  $G_R^{\text{calc}}$ . Then by constructing a master curve of  $G_R$  versus  $T$  we can determine the  $\Delta T$  required to achieve  $G_R^{\text{calc}}$ . The mechanical energy put into the sample that could be converted to heat is simply the area under the load-deflection curve less the energy due to elastic loading. The mass of material involved in shear deformation is estimated from the analysis of the images in Figure 9. By using the mechanical

energy of deformation, the mass of material in the shear band and the specific heat capacity of each material, estimates are made of the temperature increase during shear deformation (Tables 1 and 2). These estimates of temperature increase are likely to be overestimates considering Adams and Farris have shown that only 50–80% of the work of deformation is dissipated as heat during cold drawing of PC.<sup>22</sup> Even with these generous estimates, an increase in temperature does not completely account for the discrepancy between predicted and observed orientation.

### Kinematic Limit

To establish a kinematic limit for shear strain in a shear band we will consider the dimensions of the entanglement network. We will assume entanglements behave as permanent crosslinks on the timescale of these experiments. Additional assumptions include constant cross-sectional area and volume. The key parameters describing the entanglement network are,  $M_e$ , the molecular weight between entanglements,  $l_e$ , the chain contour length of a segment of molecular weight  $M_e$  and  $d$ , the entanglement mesh size (Fig. 21). The extension of a segment to its contour length represents a kinematic limit since further deformation would result in slippage at entanglement points or chain scission. Four entanglement points are deformed under shear until each adjoining chain segment reaches its maximum extension of  $l_e$ . The maximum shear strain,  $\gamma_{\max}$ , within the shear band can then be described in terms of the entanglement network parameters,

$$\gamma_{\max} = \cos^{-1} \frac{d}{l_e} \quad (10)$$

Using an approach analogous to the one outlined above, Donald and Kramer have made predictions on the maximum extension ratio one might expect in a craze based on

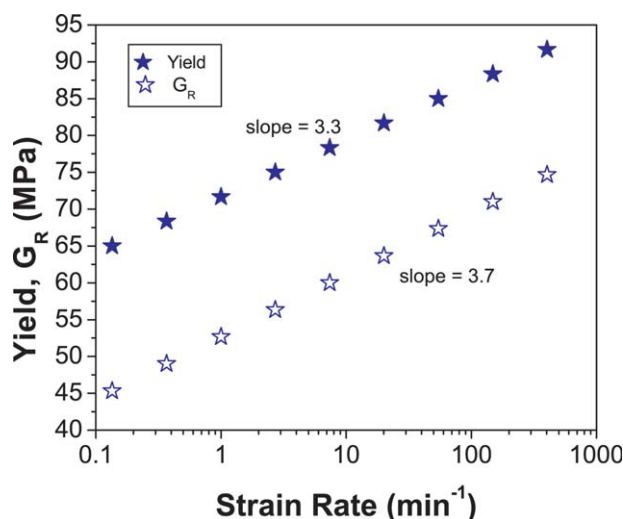


**FIGURE 22** Relative rate dependence of yield stress and strain hardening modulus for PC.

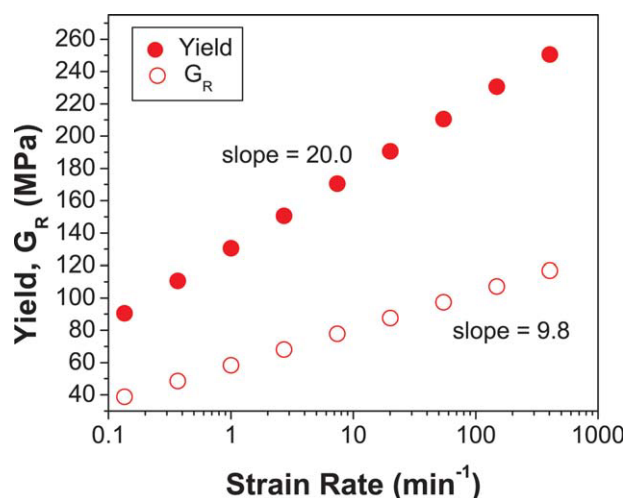


**FIGURE 23** Relative rate dependence of yield stress and strain hardening modulus for PMMA.

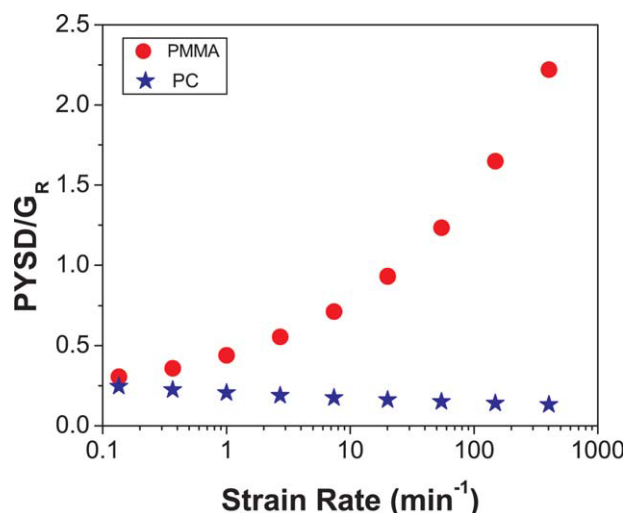


**FIGURE 24** Rate dependence of the post yield stress drop normalized by strain hardening modulus.

dimensions of the entanglement network.<sup>23</sup> Using the values for  $d$  and  $l_e$  from Donald and Kramer this predicts  $\gamma_{\max} = 1.2$  for both PC and PMMA. In Figure 10, the shear strain in PMMA increases with rate until Mode II fracture occurs. The maximum shear strain achieved prior to Mode II fracture is just below the predicted kinematic limit of 1.2. It appears that for PMMA, Mode II fracture will occur when the conditions allow the shear band to exceed the kinematic limit. At the highest rates tested, PC still produces stable shear bands and the amount of shear strain is well below the predicted kinematic limit. The highest impact speeds in this study were on the order of 4 m/s. It is interesting to note that Ravi-Chandar et al. have reported Mode II fracture in PC at impact rates exceeding 55 m/s.<sup>9</sup>

PMMA and PC differ greatly in the rate dependence of the intrinsic material properties. PMMA shows greater rate dependence for yield stress, rejuvenated stress, and strain hardening modulus. Some interesting characteristics are revealed when comparing the relative rate dependence of the properties of each material. For example, if one compares the rate dependence of  $\sigma_y$  to that of  $G_R$  in PC, the two display nearly identical trends (Fig. 22). In stark contrast is the response of PMMA. The rate dependence of  $\sigma_y$  is approximately double the rate dependence of  $G_R$  (Fig. 23). The strain hardening modulus is a measure of the material's ability to stabilize the localized strain. If a material shows a sufficient increase in  $G_R$  with increases of strain localization, the material will be able to stabilize the shear band and stable propagation will occur as seen in PC. However, if the amount of strain localization increases at a greater rate than  $G_R$ , there will be a rate above which the material is unable to stabilize the shear band and fracture will occur, as seen in PMMA. This behavior can be captured by plotting the relative rate dependence of the ratio of the post yield stress drop (PYSD), to  $G_R$  (Fig. 24). An increase in PYSD/ $G_R$  repre-

sents a greater propensity for unstable shear band growth and Mode II fracture. These trends are further supported by the finite element analysis of shear banding by Wu and van der Giessen.<sup>24</sup>

## CONCLUSIONS

The effect of rate on shear band formation was evaluated for PMMA and PC. In both polymers, the maximum shear strain in the shear band increases with rate. Mode II fracture is observed in PMMA above impact rates of 500 mm/min. The Mode II fracture toughness of PMMA is approximately seven times the Mode I fracture toughness. This suggests that if one is able to suppress Mode I fracture, whether through a superposed compressive stress or other means, the impact resistance of the material will be drastically increased. Mode II fracture was not observed in PC for the range of rates tested. The condition for shear band stability based on intrinsic material properties was developed. This theory agrees qualitatively with the shear band response of PMMA but underestimates the amount of orientation. The kinematic limit of shear strain was determined based on dimensions of the entanglement network. Mode II fracture occurs at the kinematic limit in PMMA.

## ACKNOWLEDGMENTS

The authors are grateful for the assistance of Nicholas Tsantinis and John Song. The authors acknowledge the financial support of the Army Research Laboratories and the Center for UMass/Industry Research on Polymers (CUMIRP).

## REFERENCES AND NOTES

- 1 Hsieh, A. J.; DeSchepper, D.; Moy, P.; Dehmer, P. G.; Song, J. W. Army Research Laboratories - Technical Report - 3155, **2004**.
- 2 Archer, J. S.; Lesser, A. J. *J. Appl. Polym. Sci.* **2009**, *114*, 3704–3715.
- 3 Ayatollahi, M. R.; Aliha, M. R. M. *Int. J. Solids Struct.* **2006**, *43*, 5217–5227.
- 4 Ayatollahi, M. R.; Aliha, M. R. M.; Hassani, M. M. *Mater. Sci. Eng.: A* **2006**, *417*, 348–356.
- 5 Erdogan, F.; Sih, G. C. *J. Basic Eng.* **1963**, *85*, 519–525.
- 6 Melin, S. *Int. J. Fract.* **1986**, *30*, 103–114.
- 7 Broberg, K. B. *Eng. Fract. Mech.* **1987**, *28*, 663–679.
- 8 Kalthoff, J. F. *Opt. Eng.* **1988**, *27*, 835–840.
- 9 Ravi-Chandar, K.; Lu, J.; Yang, B.; Zhu, Z. *Int. J. Fract.* **2000**, *101*, 33–72.
- 10 Rosenfield, A. R.; Kanninen, M. F. *J. Macromol. Sci. Phys.* **1973**, *7*, 609–631.
- 11 Johnson, F. A.; Radon, J. C. *J. Polym. Sci. Part A: Polym. Chem.* **1973**, *11*, 1995–2020.
- 12 Beardmore, P.; Fellers, J. *Mater. Sci. Eng.* **1970**, *5*, 120–125.
- 13 Bhattacharjee, D.; Knott, J. F. *Int. J. Fract.* **1995**, *72*, 359–381.



- 14** Ward, I. M.; Sweeney, J. *An Introduction to the Mechanical Properties of Solid Polymers*; Wiley: New York, **2004**, p 310.
- 15** Lee, S. M. *J. Reinforc. Plast. Compos.* **1999**, *18*, 1254–1266.
- 16** Kwon, H. J.; Jar, P. Y. B. *Polymer* **2005**, *46*, 12480–12492.
- 17** Haward, R. N. *Polymer* **1987**, *28*, 1485–1488.
- 18** van Melick, H. G. H.; Govaert, L. E.; Meijer, H. E. H. *Polymer* **2003**, *44*, 3579–3591.
- 19** Boyce, M. C.; Arruda, E. M. *Polym. Eng. Sci.* **1990**, *30*, 1288–1298.
- 20** Monnerie, L.; Halary, J.; Kausch, H.-H. *Intrinsic Molecular Mobility and Toughness of Polymers I*; Springer: Berlin/Heidelberg, **2005**; pp 215–372.
- 21** G'Sell, C.; Gopez, A. J. *J. Mater. Sci.* **1985**, *20*, 3462–3478.
- 22** Adams, G. W.; Farris, R. J. *J. Polym. Sci. Part B: Polym. Phys.* **1988**, *26*, 433–445.
- 23** Donald, A. M.; Kramer, E. J. *J. Polym. Sci. Part B: Polym. Phys.* **1982**, *20*, 899–909.
- 24** Wu, P. D.; van der Giessen, E. *Int. J. Solids Struct.* **1994**, *31*, 1493–1517.